UNIVERSITÉ DE GENÈVE

Archive ouverte UNIGE

https://archive-ouverte.unige.ch

Article scientifique | Article | 2022

Appendix | Open Access

This file is a(n) Appendix of:

Eustatic sea-level fall and global fluctuations in carbonate production during the Carnian Pluvial Episode

Jin, Xin; Franceschi, Marco; Martini, Rossana; Shi, Zhiqiang; Gianolla, Piero; Rigo, Manuel; Wall, Corey J.; Schmitz, Mark D.; Lu, Gang; Du, Yixing; Huang, Xiangtong; Preto, Nereo

This publication URL: https://archive-ouverte.unige.ch/unige:162137

Publication DOI: 10.1016/j.epsl.2022.117698

© This document is protected by copyright. Please refer to copyright holders for terms of use.

Eustatic sea-level fall and global fluctuations in carbonate production during the Carnian Pluvial Episode

Xin Jin [1], Marco Franceschi * [2], Rossana Martini [3], Zhiqiang Shi [1], Piero Gianolla [4], Manuel Rigo [5, 6], Corey J. Wall [7], Mark D. Schmitz [7], Gang Lu [1], Yixing Du [1], Xiangtong Huang [8], Nereo Preto [5]

1. State Key Laboratory of Oil and Gas Reservoir Geology and Exploitation and Key Laboratory of Deep-time Geography and Environment Reconstruction and Applications of Ministry of Natural Resources, Chengdu University of Technology, Chengdu 610059, China

2. Department of Mathematics and Geosciences, University of Trieste, via Weiss, 2, 34128 Trieste, Italy

3. Department of Earth Sciences, University of Geneva, 13 Rue des Maraîchers, 1205 Geneva, Switzerland

4. Department of Physics and Earth Sciences, Università degli Studi di Ferrara, Via Saragat, 1, Ferrara 44100, Italy

5. Dipartimento di Geoscienze, Università degli Studi di Padova, Via G. Gradenigo 6, Padova, Italy

6. Istituto di Geoscienze e Georisorse–CNR, Via G. Gradenigo 6, Padova, Italy

7. Department of Geosciences, Boise State University, 1910 University Drive, Boise, ID 83725-1535, U.S.A.

8. State Key Laboratory of Marine Geology, Tongji University, Siping Road, Shanghai, 200092, China

*Corresponding author: mfranceschi@units.it

1. Methods

1.1. Petrological studies

Sample preparation was carried out at the Institute of Sedimentary Geology of the Chengdu University of Technology (China) and Department of Geosciences of the University of Padova (Italy). A total of 69 bulk rock samples were collected at the Hanzeng section and were processes to obtain standard 30 μm thin sections. Thin sections were investigated under a polarizing optical microscope, and these were studied and photographed with a polarizing microscope at the Institute of Sedimentary Geology of the Chengdu University of Technology. Microfacies textures were described according to Dunham's (1962) classification, supplemented by Embry and Klovan (1971).

1.2. Conodonts

We collected 8 rock samples for conodont investigation from the Hanzeng section (Fig. 2 in main text), each weighing about 2-3 kg. Rock samples were crushed into small pieces of about 2-3 cm and then dissolved in formic acid (7%). After that, the residues were washed, sieved (100 μm), and dried at 40° C in an oven. Residues were separated into heavy and light fractions by non-toxic heavy liquid (sodium polytungstate). The resulting residues were collected and then examined under a microscope. The specimens are photographed and kept in the Department of Geoscience, University of Padova (Italy).

1.3. Foraminifers

Seventeen samples (A to Q) were collected from the base up to ca. 50 m of the Hanzeng section (Fig. 2 in main text). A total of sixteen standard (30 μm thick) thin sections of size 47 mm × 28 mm were made. Samples were taken every 2 m in the first 28 m of the section, corresponding to the Tianjingshan Fm. and the base of the Ma'antang Fm., which age could not be constrained by conodonts as they were missing because of the shallow water depositional environment. Thin sections were investigated under a polarizing optical microscope, and microfacies textures were described according to Dunham's (1962) classification, supplemented by Embry and Klovan (1971).

1.4. LA-ICP-MS method

Detrital zircons were extracted from bulk samples at laboratory of the Langfang Sincerity Geological Service Co., Ltd (Hebei, China), using conventional heavy liquid and magnetic separation techniques. More than 1000 grains from each sample were picked, from which about 250 random grains were mounted in epoxy resin under the binocular microscope. Prior to geochronological analysis, the polished epoxy disks were imaged using cathodoluminescence (CL) in order to locate proper analytical spots in zircon oscillatory zoning. U-Pb dating was performed by LA-ICP-MS at the State Key Laboratory of Marine Geology, Tongji University, China. The laser system was an Agilent 7900 quadrupole ICP-MS coupled to a Resonetics M50 193 nm excimer laser ablation system. The laser beam was set to shot at 6 Hanzeng with a spot size of 26 μm, and the laser energy density was 4 J/cm $^{-2}$. The ablated material was then carried to the ICP-MS with a He-Ar gas mixture. Each analysis incorporated 20 s of gas blank followed by 50 s of data acquisition. Zircon 91500 (1065.4 ± 0.3 Ma) (Wiedenbeck et al., 1995) was used as an external standard, and was analyzed twice every seven analyses. Accuracy was monitored by zircon Plešovice with an age of 337.1 ± 0.4 Ma (Sláma et al., 2008). U-Th-Pb isotopic ratios were calculated using ICPMSDataCal (Liu et al., 2010) followed by the common Pb correction method of Andersen (2002). A total of 83 grains were analyzed, and the age data are reported at 1σ level of uncertainty. The best ages were extracted from a 90% concordant subset, wherein the ^{206}Pb/^{238}U and ^{207}Pb/^{206}Pb ages were adopted for zircons younger and older than 1000 Ma, respectively (Compston et al., 1992). In this study, our age results and other published data were visualized as kernel density estimation and histograms using DensityPlotter (Vermeesch, 2012).

1.5. CA-ID-TIMS method

Grains were selected from provided CL images and laser ablation data. From these compiled images, grains with consistent and uniform CL patterns and in-situ U-Pb dates were designated for further isotopic analysis. Individual zircon grains were plucked from epoxy mounts and placed in a muffle furnace at 900°C for 60 hours in quartz beakers to anneal minor radiation damage, and to prepare the crystals for subsequent chemical abrasion (Mattinson, 2005). U-Pb geochronology methods for isotope dilution thermal ionization mass spectrometry follow those previously published by Davydov et al. (2010) and Schmitz and Davydov (2012). Zircon crystals were subjected to a modified version of the chemical abrasion method of Mattinson (2005), whereby single crystal fragments plucked from grain mounts were individually abraded in a single step with concentrated HF at 190°C for 12 hours. All analyses were undertaken on crystals previously mounted, polished and imaged by CL, and selected on the basis of zoning patterns. U-Pb dates and uncertainties for each analysis were calculated using the algorithms of Schmitz and Schoene (2007) and the U decay constants of Jaffey et al. (1971). Uncertainties are based upon non-systematic analytical errors, including counting statistics, instrumental fractionation, tracer and blank subtraction. These error estimates should be considered when comparing our $^{206}Pb/^{238}U$ dates with those from other laboratories that used tracer solutions calibrated against the EARTHTIME gravimetric standards. When comparing our dates with those derived from other decay schemes (e.g., $^{40}Ar/^{39}Ar$, ^{187}Re-^{187}Os), the uncertainties in tracer calibration (0.03%; Condon et al., 2015; McLean et al., 2015) and U decay constants (0.108%; Jaffey et al., 1971) should be added to the internal error in quadrature. Quoted errors for calculated weighted means are thus of the form ±X(Y) [Z], where X is solely analytical uncertainty, Y is the combined analytical and tracer uncertainty, and Z is the combined analytical, tracer and ^{238}U decay constant uncertainty.

1.6. $\delta^{13}C$ and $\delta^{18}O$ analyses

One hundred and five samples were collected from the Hanzeng section. Samples were cleaned in an ultrasonic bath for 15 seconds to remove surface contamination, and washed by deionized water. Ca. 2 mg of powder were obtained by a hand-held drill from diagenetically unaltered portions of freshly broken samples.

Ca. 0.2 and 0.35 mg of 66 samples were weighted into exetainer glass vials, which were flushed with high-purity He less than 24 h before the analysis. CO_2 was produced at 70 °C by complete reaction with 99% H_3PO_4 in a Delta V Advantage Isotopic Ratio Mass Spetrometer linked to a Gasbench II device at the Department of Geosciences of the University of Padova. The measured raw $\delta^{13}C$ and $\delta^{18}O$ were normalized against an internal standard (white Carrara calcite marble Maq 1: $\delta^{13}C$ = 2.58‰; $\delta^{18}O$ = 1.15‰ VPDB). The standard deviations of the analyses of a quality assurance standard are less than 0.07‰ for $\delta^{13}C$, and less than 0.10 ‰ for $\delta^{18}O$ during the period of the analyses.

A total of 39 samples were analyzed at College of Earth Sciences, Chengdu University of Technology. The powders were reacted with 99% H_3PO_4 at 50°C in a GasBench II attached to a Thermo Finnigan MAT 253 Mass Spectrometer. Analytical reproducibility by repeated analyses of international reference standards ANU-M1 ($\delta^{13}C$= +1.36‰, $\delta^{18}O$= -6.14‰), ANU-M2 ($\delta^{13}C$= +2.81‰, $\delta^{18}O$= -7.34‰) and ANU-PRM2 ($\delta^{13}C$= +0.71‰, $\delta^{18}O$= -17.41‰). Analytical uncertainties on $\delta^{13}C_{carb}$ and $\delta^{18}O_{carb}$ analyses are better than 0.08‰ and 0.06‰, respectively. All isotopic values are reported with respect to the VPDB (Vienna Pee Dee Belemnite) standard.

2. Petrology of the Tianjingshan and Ma'antang formations

2.1. Uppermost Tianjingshan Formation

At Hanzeng, the grayish white, thick-bedded carbonates of uppermost

Tianjingshan Fm. are generally characterized by abundant microbialites (Fig. 2 and Fig. S2A). Karst 1 (~11.3 m) is within the uppermost Tianjingshan Fm. A bentonite layer, with thickness of ~ 20 cm, overlies Karst 1 surface which is also characterized by iron oxide coatings (Fig. S2B). Darker limestones fill in the irregular karst depressions (Fig. S2B). The boundary between Tianjingshan and Ma'antang formations is defined by the Karst 2 (~25 m) which is marked by 5-10 cm thick paleosol with calcretes (Fig. S2C).

Below the Karst 1, the Tianjingshan Fm. is dominated by five microfacies: E1, E2, E3, F1 and F2 (Fig. 2 in main text). Microfacies E1 are stromatolites or stromatolitic breccia (Fig. SI1-E1), with mm-scale laminae of uniform or clotted peloidal micrite. E2 is a bioturbated mudstone-wackestone (Fig. SI1-E2), very fine skeletal fragments and pervasive bioturbation are seen in the thin section. E3 is an intraclastic grainstone, where the intraclasts are made of microbial carbonate (Fig. SI1-E3), and skeletal grains are rare. F1 is a thrombolitic microbial boundstone, characterized by micritic carbonates with clotted peloidal fabric, and skeletal grains are rare (Fig. SI1-F1). F2 is an oncoidal floatstone (Fig. SI1-F2). Oncoids are dominant, up to 1 cm in diameter, in a matrix of grainstone with dominant microbial intraclasts.

Between Karst 1 and Karst 2, stromatolites are present but less abundant than in underlying layers, instead the oncolities and skeletal grains are dominant (Fig. 2 in main text). Seven microfacies are found, i.e., E1, E2, E3, D1, D2, D3, D4, F2. Microfacies D1 is a foraminiferal packstone-grainstone (Fig. SI1-D1). Aragonitic foraminifers are dominant. D2 is a packstone-floatstone with mollusks (Fig. SI1-D2). D3 microfacies is a wackestone-packstone with ostracods (Fig. SI1-D3). D4 is a compacted rudstone or breccia which is made of cm-scale, partially lithified fragments of stromatolite (Fig. SI1-D4).

2.2. Lower part of the Ma'antang Formation

The overlying Ma'antang Fm. (above ~25 m) is made of ten microfacies associations, A1, A2, A3, B1, B2, C1, C2, C3, D2 and D3. The rocks are generally gray with darker patches (Fig. S2A). From Karst 2 to the off-white wackestone-packstone interbedded with laminated ostracod layers (~26.5 m), the sediments can be classified to the D2 and D3 microfacies associations (Fig. 2), and ostracods are abundant (Fig. S2D).

From ~26.5 m to ~32.7 m levels, A2, C3, C1 are present in stratigraphic order. The A2 microfacies association is bioclastic grainstone (Fig. SI1-A2). Skeletal grains are diverse and well sorted. Ooids and intraclasts may also occur. C3 is characterized by fine-grained packstone to grainstone with small and often fragmented skeletal grains, intraclasts and peloids (Fig. SI2-C3). C1 is marked by wackestone or packstone with abundant peloids and highly fragmented (Fig. SI2-C1), small skeletal grains. From ~32.7 m to ~64.5 m levels, the carbonate rocks are mainly characterized by fine carbonates. Chert nodules locally occur (Fig. S2E). Thin-bedded wackestone/packstone, represent the most common lithofacies of this interval. C1, C2 and C3 are recognized in this interval. C2 is fine-grained wackestone or packstone with dominant siliceous sponge spicules, usually replaced by calcite (Fig. SI2-C2). C1 and C2 are the dominant facies in this interval. From 64.5 m to the top, the carbonates are mainly composed of microbialites (B1 and B2). B1 is sponge rudstone-floatstone (Fig. SI2-B1). Floatstones to rudstones with cm-scale reef builders, mostly calcareous sponges and, more rarely, calcimicrobes (e.g., *Cayeuxia*). Algae are visible. B2 is composed of bindstones to framestones with mostly calcareous sponges (Fig. SI2-B2), coated by microbial envelopes or growing along with thrombolitic microbialites and rarer calcimicrobes. Siliceous sponge spicules, bounded by thrombolites microbial carbonate with clotted peloidal fabric, are locally occurring. At the topmost of the Ma'antang Fm., A1, A2, A3 microfacies associations are found. A1 is oolitic grainstone (Fig. SI2-A1; Fig. SI2-O), in dm-m scale beds, well sorted. Ooids are radial and may be as large as 1 mm in diameter. Coral or sponge colonies occur sparsely. The character of oolites are similar to the description of oolites in the Ma'antang Fm. from Jin et al. (2018). A3 is bioclastic floatstone (Fig. SI2-A3), and is very similar to A2, but also includes larger, worn, strongly micritized and rounded fragments of reef builders.

3. Carbon stable isotopes: Diagenetic screening and explanations

Influence of diagenetic alteration of $\delta^{13}C$ record from Hanzeng section has been assessed by correlation analysis. A low correlation between $\delta^{13}C$ and $\delta^{18}O$ values is interpreted as an element speaking in favor of low diagenetic overprint on bulk-carbonate isotopes chemistry (e.g., Sun et al., 2019). The $\delta^{13}C$ and $\delta^{18}O$ values of the Hanzeng section exhibit a significant correlation (R = 0.386, P<0.001, N = 105; Fig. S7). However, when only the isotope data falling in the range of those obtained from well-persevered Tethysian Carnian brachiopods shells (Korte et al., 2005), correlation between $\delta^{13}C_{org}$ and $\delta^{13}C_{carb}$ values drops (R = 0.166, P>0.05, N = 60; Fig. S7). Such data points are therefore considered as not significantly altered by diagenesis and are shown as black dots in Figure 2. If isotope data falling in a $\delta^{13}C_{org}$ vs $\delta^{13}C_{carb}$ cross-plot outside the range from Carnian brachiopods (Korte et al., 2005; marked as red filled triangles in the Fig. S7) are excluded, the hNCIE3 found above Karst 2 surface and culminating at meter 30 persists (Fig. 2), an evidence indicating that the feature reflects changes in the $\delta^{13}C$ of Carnian sea-water.

Figure captions

Fig. S1. Correlation of $\delta^{13}C$ records, Hg/TOC ratios and initial osmium isotope ratios ($^{187}Os/^{188}Os$) from eastern Tethys (Hanzeng, this study; Nanpanjiang Basin, Sun et al., 2016), western Tethys ($\delta^{13}C$, Dal Corso et al., 2018; Hg/TOC, Mazaheri-Jorari et al., 2021), Panthalassa (Tomimatsu et al., 2021) and Pangaea (Jiyuan Basin, Lu et al., 2021). J.1 = Julian 1; J. 2 = Julian 2; T.1 = Tuvalian 1; T.2 = Tuvalian 2; CPE = Carnian Pluvial Episode; NCIE = Negative carbon isotopic excursions.

Fig. S2. Representative field photographs of upper Tianjingshan to Ma'antang formations in Hanzeng section. **A**). Panorama view of lower to middle parts of the Hanzeng section. The two karsts are marked by yellow dashed lines. **B**). Close up of the karstic clay (Karst 1) and adjoining layers. The purple star marked the position of zircon sample at Hanzeng. **C**). Close up of Karst 2 and overlying bioclastic layer. Within the karstic clay, off-white and irregular calcretes are abundant and are showed by red arrow. **D**). Off-white wackestone-packstones interbedded with laminated ostracod layers; ostracod layers are marked by red arrows. **E**). Close-up of chert nodules from ~ 60 m section height (red arrows). The hammer and marker are ca. 30 cm and 14.5 cm long, respectively.

Fig. S3. Facies model of the Hanzeng section. FWWB = fair weather wave base. A, B, C and D refer to the facies associations (See the Supplemental Dataset).

Fig. S4. Scanning Electron Microscope photomicrographs of the key conodont elements from Hanzeng section. (**1**) *Paragondolella* aff. *P. foliata*; **(2-3**) *Hayashiella tuvalica*; (**4**) *Paragondolella oertlii*; (**5**) *Paragondolella maantangensis*. For each specimen: (a) upper view, (b) lower view, (c) lateral view. The Color Alteration Index of these conodonts is 1. All scale bars = 200 μm.

Fig. S5. Benthic foraminifers from Hanzeng section. The specimens are shown in stratigraphic order, from bottom to top (see Fig. 2 in main text). (**1**) Recrystallised *Triadodiscus eomesozoicus* (sampl. N-1); (**2**) Nodosarid (sampl. L-2); (**3**) *Variostoma pralongense* (sampl. O-3); (**4, 5**) *Agathammina iranica* (sampl. 4: O-4; 5: P-1); (**6**) *Gsolbergella spiroloculiformis* (sampl. O-2); (**7-9**) *Aulotortus impressus* (sampl. 7: J-1; 8: J-5; 9: J-6); (**10, 11**) "*Trochammina*" sp. (sampl. 10: G-1; 11: H-4); (**12**) "*Valvulina*" *azzouzi* (sampl. F-5); (**13**) *Endotriada tyrrhenica* (sampl. I-3); (**14**)

Endotriada ?tyrrhenica (sampl. F-1); (**15-18, 24**) *Parvalamella friedli* (sampl. 15: C-6; 16: B-4; 17: E-1; 18: E-5; 24: C-8); (**19**) Foraminifer indet. (sampl. B-7); (**20, 25**) “*Trochammina” alpina* (sampl. 20: B-10; 25: C-7); (**21**) *Aulotortus sinuosus* (sampl. B-6); (**22**) *Gaudrina triadica* (sampl. E-7); (**23**) Encrusting foraminifer (B-2). All scale bars = 100 μm.

Fig. S6. A) Representative cathodoluminescence (CL) images of zircons from Hanzeng section. Volcanic zircons show prismatic or euhedral morphology. **B)** The weighted mean age of zircons reported at 2σ level of uncertainty and obtained from LA-ICP-MS analysis. **C)** Concordia plots for 53 zircons grains from sample Hanzeng. **D)** Weighted mean age of zircons reported at 2σ level of uncertainty and obtained from CA-ID-TIMS analysis. **E)** Concordia plots for eight zircons grains.

Fig. S7. Cross-plot of carbonate $\delta^{13}C$ and $\delta^{18}O$ in the Hanzeng section. Different symbols are corresponded to different analytical samples (bottom legend). Orange dots represent isotopic data from bulk rock which are not specialized. The orange triangles represent isotopic values of the hNCIE3, and their $\delta^{18}O$ values are all located in isotopic variation of Carnian well brachiopods (Korte et al., 2005), while some $\delta^{13}C$ values are outside the range which are suggested to additional input of $\delta^{13}C$- depleted carbon source (gray band).

Fig. SI1. Macrofacies of Middle Triassic to Upper Triassic in the Hanzeng section. The detailed descriptions of the macrofacies are showed in the Supplemental Dataset. **E1**).

Stromatolite and stromatolitic breccia. The stromatolites are labeled to St. The stromatolitic breccia are showed by yellow arrows. **E2**). Bioturbated mudstone-wackestone. The burrow pores are marked by red dashed lines. **E3**). Intraclastic grainstone. Intraclasts are mainly consist of microbial carbonates (red arrows). **F1**). Thrombolitic microbial boundstone. The lower part of the thin section is mainly composed of micrites. The upper part of the thin section mainly consists of clotted peloidal micrites. The framework cavities (red arrows) are abundant and often associated with geopetal infilling in the upper part. **F2**). Oncoidal floatstone. The diameters of oncoids (On) are up to 1 cm. **D1**). Foraminiferal packstone-grainstone. Aragonitic foraminifers (Fo) are dominant. Details are shown in yellow square. **D2**). Packstone-floatstone with mollusks. The grains are mainly composed of bivalves (Bi), gastropods (Ga) and foraminifers (Fo) (also seen in yellow square). **D3**). Wackestone-packstone with ostracods. An oligotypic skeletal association dominated by ostracods. Details are shown in yellow square. **D4**). Intraclast rudstone (flat-pebble breccia). Intraclasts are mainly made of lithified fragments of stromatolite (St). Fragments of bivalve (Bi) are seen. **A2**). Bioclastic grainstone. Well sorted grainstone, and bioclasts are diverse. All scale bars = 1cm.

Fig. SI2. Continued macrofacies of Middle Triassic to Upper Triassic in the Hanzeng section. **C3**). Bioclastic packstone-grainstone. Skeletal grains are small and fragmented. Details are shown in yellow square. **C1**). Wackestone-packstone with fragmented skeletal grains. Skeletal grains are small and highly fragmented. Intergranular spaces are filled with carbonate muds. Details are shown in yellow square. **C2**). Spiculitic wackestone-packstone. Siliceous sponge spicules (green arrows in yellow square) are dominant and usually replaced by calcites. Small peloids are also visible (red arrows in yellow square). **B1**). Sponge rudstone-floatstone. The large grains are dominated by calcareous sponges (Cs). The algae (Al) are also visible. They often have a thick microbial coating (Mc). **B2**). Sponge-microbial boundstone. Calcareous sponges (Cs) are locally coated by microbial envelopes (Me) or growing along with thrombolitic microbialites (Th). Algae and worm tubes (Wt) locally occur. **A1**). Oolitic grainstone. Ooids are mainly radial and well sorted. **O**). Oolitic grainstones occur at 105 to 110 m height in Fig. 2 in main text. **A3**). Bioclastic floatstone. Unidentified larger gains, corals, calcareous sponges (Cs), algae (Al), are often coated by microbial envelopes and are embedded in a fine carbonate matrix with mollusks, foraminifers, brachiopods, echinoderms, peloids and ooids. All white bars = 0.5 cm.

References

Andersen, T., 2002. Correction of common lead in U–Pb analyses that do not report ^{204}Pb. Chemical Geology, 192, 59-79. https://doi.org/10.1016/S0009-2541(02)00195-X

Compston, W., Williams, I.S., Kirschvink, J.L., Zichao, Z., Guogan, M.A., 1992. Zircon U-Pb ages for the Early Cambrian time-scale. Journal of the Geological Society, 149(2), 171-184. https://doi.org/10.1144/gsjgs.149.2.0171

Condon, D.J., Schoene, B., McLean, N.M., Bowring, S.A., Parrish, R.R., 2015. Metrology and traceability of U–Pb isotope dilution geochronology (EARTHTIME Tracer Calibration Part I). Geochimica et Cosmochimica Acta, 164, 464-480. https://doi.org/10.1016/j.gca.2015.05.026

Dal Corso, J., Gianolla, P., Rigo, M., Franceschi, M., Roghi, G., Mietto, P., Manfrin, P., Raucsik, B., Budai, T., Jenkyns, H.C., Reymond, C.E., Caggiati, M., Gattolin, G., Breda, A., Merico, A., Preto, N., 2018. Multiple negative carbon-isotope excursions during the Carnian Pluvial Episode (Late Triassic). Earth-Science Reviews, 185, 732-750. https://doi.org/10.1016/j.earscirev.2018.07.004

Davydov, V.I., Crowley, J.L., Schmitz, M.D., Poletaev, V.I., 2010. High‐precision U‐Pb zircon age calibration of the global Carboniferous time scale and Milankovitch band cyclicity in the Donets basin, eastern Ukraine. Geochemistry, Geophysics, Geosystems, 11(2). https://doi.org/10.1029/2009GC002736

Dunham, R.J., 1962. Classification of carbonate rocks according to depositional texture. AAPG Memoir, 1, 108-121. https://doi.org/10.1306/M1357

Embry, A.F., Klovan, J.E., 1971, A Late Devonian reef tract on Northeastern Banks Island, NWT. Bulletin of Canadian petroleum geology, 19, 730-781. https://doi.org/10.35767/gscpgbull.19.4.730

Jaffey, A.H., Flynn, K.F., Glendenin, L.E., Bentley, W.T., Essling, A.M., 1971. Precision measurement of half-lives and specific activities of U^{235} and U^{238}. Physical review C, 4(5), 1889. https://doi.org/10.1103/PhysRevC.4.1889

Jin, X., McRoberts, A.C., Shi, Z.Q., Mietto, P., Rigo, M., Roghi, G., Manfrin, S., Franceschi, M., Preto, N., 2019. The aftermath of the CPE and the Carnian/Norian transition in northwestern Sichuan Basin, South China. Journal of the Geological Society, 176, 179-196. https://doi.org/10.1144/jgs2018-104

Korte, C., Kozur, H.W., Veizer, J., 2005. $\delta^{13}C$ and $\delta^{18}O$ values of Triassic brachiopods and carbonate rocks as proxies for coeval seawater and palaeotemperature. Palaeogeography, palaeoclimatology, palaeoecology, 226, 287-306. https://doi.org/10.1016/j.palaeo.2005.05.018

Liu, Y., Hu, Z., Zong, K., Gao, C., Gao, S., Xu, J., Chen, H., 2010. Reappraisement and refinement of zircon U-Pb isotope and trace element analyses by LA-ICP-MS. Chinese Science Bulletin, 55, 1535-1546. https://doi.org/10.1007/s11434-010-3052-4

Lu, J., Zhang, P., Dal Corso, J., Yang, M., Wignall, P. B., Greene, S. E., Shao, L., Lyu, D., Hilton, J., 2021. Volcanically driven lacustrine ecosystem changes during the Carnian Pluvial Episode (Late Triassic). Proceedings of the National Academy of Sciences. 118(40). https://doi.org/10.1073/pnas.2109895118

Mattinson, J.M., 2005. Zircon U–Pb chemical abrasion ("CA-TIMS") method: combined annealing and multi-step partial dissolution analysis for improved precision and accuracy of zircon ages. Chemical Geology, 220(1-2), 47-66. https://doi.org/10.1016/j.chemgeo.2005.03.011

Mazaheri-Johari, M., Gianolla, P., Mather, T.A. Frieling, J., Chu, D., Dal Corso, J. 2021. Mercury deposition in Western Tethys during the Carnian Pluvial Episode (Late Triassic). Scientific Reports. 11, 17339. https://doi.org/10.1038/s41598-021-

96890-8

McLean, N.M., Condon, D.J., Schoene, B., Bowring, S.A., 2015. Evaluating uncertainties in the calibration of isotopic reference materials and multi-element isotopic tracers (EARTHTIME Tracer Calibration Part II). Geochimica et Cosmochimica Acta, 164, 481-501. https://doi.org/10.1016/j.gca.2015.02.040

Schmitz, M.D., Schoene, B., 2007. Derivation of isotope ratios, errors, and error correlations for U‐Pb geochronology using 205Pb‐235U‐(233U)‐spiked isotope dilution thermal ionization mass spectrometric data. Geochemistry, Geophysics, Geosystems, 8(8). https://doi.org/10.1029/2006GC001492

Sláma, J., Košler, J., Condon, D.J., Crowley, J.L., Gerdes, A., Hanchar, J.M., Horstwood, M.S.A., Morris, G.A., Nasdala, L., Norberg, N., Schaltegger, U., Schoene, B., Tubrett, M.N., Whitehouse, M.J., 2008. Plešovice zircon — a new natural reference material for U–Pb and Hf isotopic microanalysis. Chemical Geology, 249, 1-35. https://doi.org/10.1016/j.chemgeo.2007.11.005

Sun, Y. D., Wignall, P.B., Joachimski, M.M., Bond, D.P.G., Grasby, S.E., Lai, X.L., Wang, L.N., Zhang, Z.T., Sun, S., 2016. Climate warming, euxinia and carbon isotope perturbations during the Carnian (Triassic) Crisis in South China. Earth and Planetary Science Letters, 444, 88-100. https://doi.org/10.1016/j.epsl.2016.03.037

Sun, Y. D., Richoz, S., Krystyn, L., Zhang, Z. T., Joachimski, M. M., 2019. Perturbations in the carbon cycle during the Carnian Humid Episode: carbonate carbon isotope records from southwestern China and northern Oman. Journal of the Geological Society, 176(1), 167-177.

Tomimatsu, Y., Nozaki, T., Sato, H., Takaya, Y., Kimura, J. I., Chang, Q., Naraoka, H., Rigo, M., Onoue, T., 2021. Marine osmium isotope record during the Carnian “pluvial episode” (Late Triassic) in the pelagic Panthalassa Ocean. Global and Planetary Change, 197, 103387. https://doi.org/10.1016/j.gloplacha.2020.103387

Vermeesch, P., 2012. On the visualisation of detrital age distributions. Chemical Geology, 312, 190-194. https://doi.org/10.1016/j.chemgeo.2012.04.021

Wiedenbeck, M., Alle, P., Corfu, F., Griffin, W.L., Meier, M., Oberli, F., Von Quadt, A., Roddick, J.C., Spiegel, W., 1995. Three natural zircon standards for U-Th-Pb, Lu-Hf, trace element and REE analyses. Geostandards Newsletter, 19, 1-24. https://doi.org/10.1111/j.1751-908X.1995.tb00147.x

CA-TIMS U-Pb isotopic data

	Compositional Parameters						Radiogenic Isotope Ratios								Isotopic Ages					
Sample (a)	Th/U (b)	^{206}Pb* x10^{-13} mol (c)	mol % ^{206}Pb* (c)	Pb*/Pb$_c$ (c)	Pb$_c$ (pg) (c)	^{206}Pb/^{204}Pb (d)	^{208}Pb/^{206}Pb (e)	^{207}Pb/^{206}Pb (e)	% err (f)	^{207}Pb/^{235}U (e)	% err (f)	^{206}Pb/^{238}U (e)	% err (f)	corr. coef.	^{207}Pb/^{206}Pb (g)	± (f)	^{207}Pb/^{235}U (g)	± (f)	^{206}Pb/^{238}U (g)	± (f)
HZ-K2																				
z1	0,759	0,2829	0,976	13,3	0,57	766	0,241	0,05097	0,6	0,26477	0,6	0,03769	0,060	0,728	238,31	13,78	238,50	1,36	**238,52**	**0,14**
z2	0,737	0,2535	0,988	26,2	0,26	1495	0,234	0,05087	0,3	0,26413	0,4	0,03767	0,049	0,584	234,00	7,67	237,99	0,76	**238,40**	**0,11**
z3	0,874	0,1912	0,987	25	0,21	1393	0,277	0,05102	0,3	0,26495	0,4	0,03768	0,054	0,563	240,71	8,06	238,65	0,80	**238,44**	**0,13**
z4	0,667	0,3182	0,989	27,9	0,30	1623	0,212	0,05097	0,3	0,26469	0,3	0,03768	0,049	0,524	238,35	7,54	238,44	0,74	**238,45**	**0,11**
z5	0,760	0,1540	0,977	13,6	0,30	781	0,241	0,05115	0,6	0,26567	0,6	0,03769	0,066	0,677	246,62	13,80	239,23	1,37	**238,47**	**0,16**
z6	0,625	0,3529	0,989	27,2	0,33	1599	0,198	0,05094	0,3	0,26449	0,3	0,03767	0,040	0,642	237,09	6,57	238,28	0,66	**238,40**	**0,09**
z7	0,864	0,0669	0,943	5,4	0,34	316	0,274	0,05075	1,6	0,26348	1,7	0,03767	0,147	0,712	228,57	36,71	237,46	3,58	**238,36**	**0,34**
z8	0,646	0,1019	0,968	9,4	0,28	559	0,205	0,05093	1,0	0,26436	1,1	0,03766	0,099	0,650	236,57	22,84	238,18	2,23	**238,34**	**0,23**

Weighted Mean Date Calculations

HZ-K2

^{206}Pb/^{238}U ± random (+tracer) [+λ			**MSWD**	**prob. Fit**
238,430	± 0.047 (0.13) [0.28]	**± 2s int.**	**0,51**	0,831
	± 0.04 (0.12) [0.28]	**± 95% c.i**	**n =** 8	

*** 95% conf. int. = 2s * Student's T * (MSWD)^0.5**

(a) z1, z2 etc. are labels for single zircon crystal fragments annealed and chemically abraded after Mattinson (2005); **bold** indicates result used in weighted mean calculations.
(b) Model Th/U ratio iteratively calculated from the radiogenic 208Pb/206Pb ratio and 206Pb/238U age.
(c) Pb* and Pbc represent radiogenic and common Pb, respectively; mol % ^{206}Pb* with respect to radiogenic, blank and initial common Pb.
(d) Measured ratio corrected for spike and fractionation only. Fractionation estimated at 0.16 +/- 0.03 %/a.m.u. for Daly analyses, based on analysis of NBS-981 and NBS-982.
(e) Corrected for fractionation, spike, and common Pb; up to 0.6 pg of common Pb was assumed to be procedural blank: 206Pb/204Pb = 18.042 ± 0.61%; 207Pb/204Pb = 15.537 ± 0.52%; 208Pb/204Pb = 37.686 ± 0.63% (all uncertainties 1-sigma). The remainder of common Pb was subtracted using the composition of coexisting sanidine feldspar: 206Pb/204Pb = 18.809 ± 0.017%; 207Pb/204Pb = 15.719 ± 0.014%; 208Pb/204Pb = 39.709 ± 0.025% (all uncertainties 1-sigma).
(f) Errors are 2-sigma, propagated using the algorithms of Schmitz and Schoene (2007).
(g) Calculations are based on the decay constants of Jaffey et al. (1971). 206Pb/238U and 207Pb/206Pb ages corrected for initial disequilibrium in 230Th/238U using Th/U [magma] = 3.

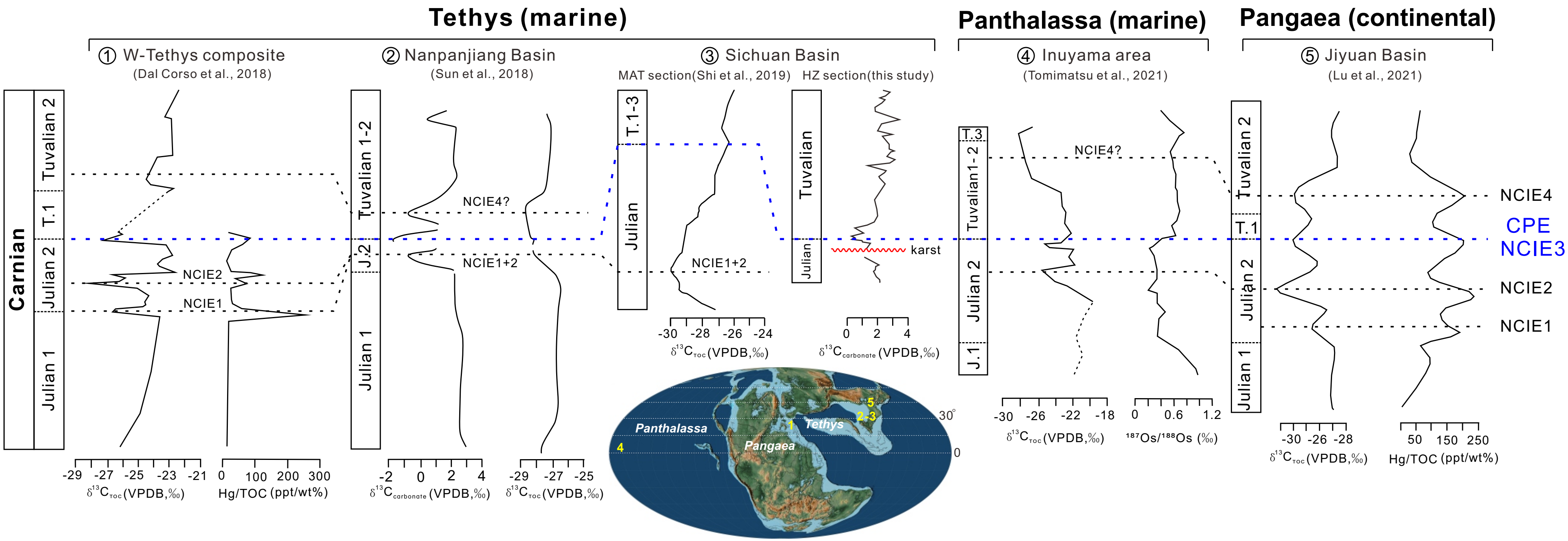

Tethys (marine)
Panthalassa (marine)
Pangaea (continental)
① W-Tethys composite
(Dal Corso et al., 2018)
② Nanpanjiang Basin
(Sun et al., 2018)
③ Sichuan Basin
MAT section(Shi et al., 2019)
HZ section(this study)
④ Inuyama area
(Tomimatsu et al., 2021)
⑤ Jiyuan Basin
(Lu et al., 2021)
Carnian
Tuvalian 2
T.1
Julian 2
Julian 1
Tuvalian 1-2
J.2
T.1-3
Julian
Tuvalian
T.3
Tuvalian1-2
J.1
NCIE1
NCIE2
NCIE4?
NCIE1+2
NCIE4
CPE
NCIE3
karst
$\delta^{13}C_{TOC}$ (VPDB,‰)
Hg/TOC (ppt/wt%)
$\delta^{13}C_{carbonate}$ (VPDB,‰)
$^{187}Os/^{188}Os$ (‰)
Panthalassa
Tethys
Pangaea
30°
0

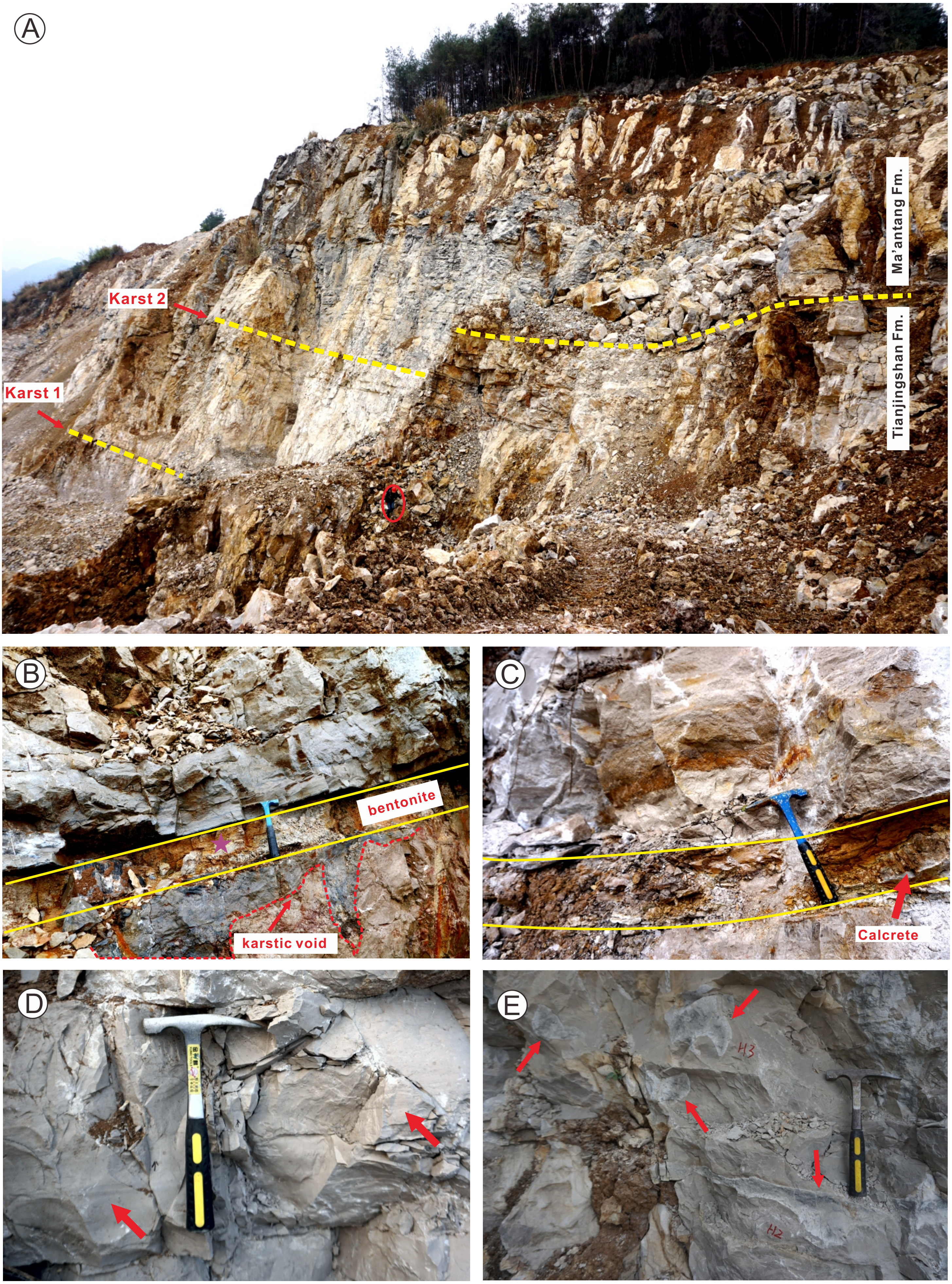

A
Karst 2
Karst 1
Ma'antang Fm.
Tianjingshan Fm.
B
bentonite
karstic void
C
Calcrete
D
E
H3
H2

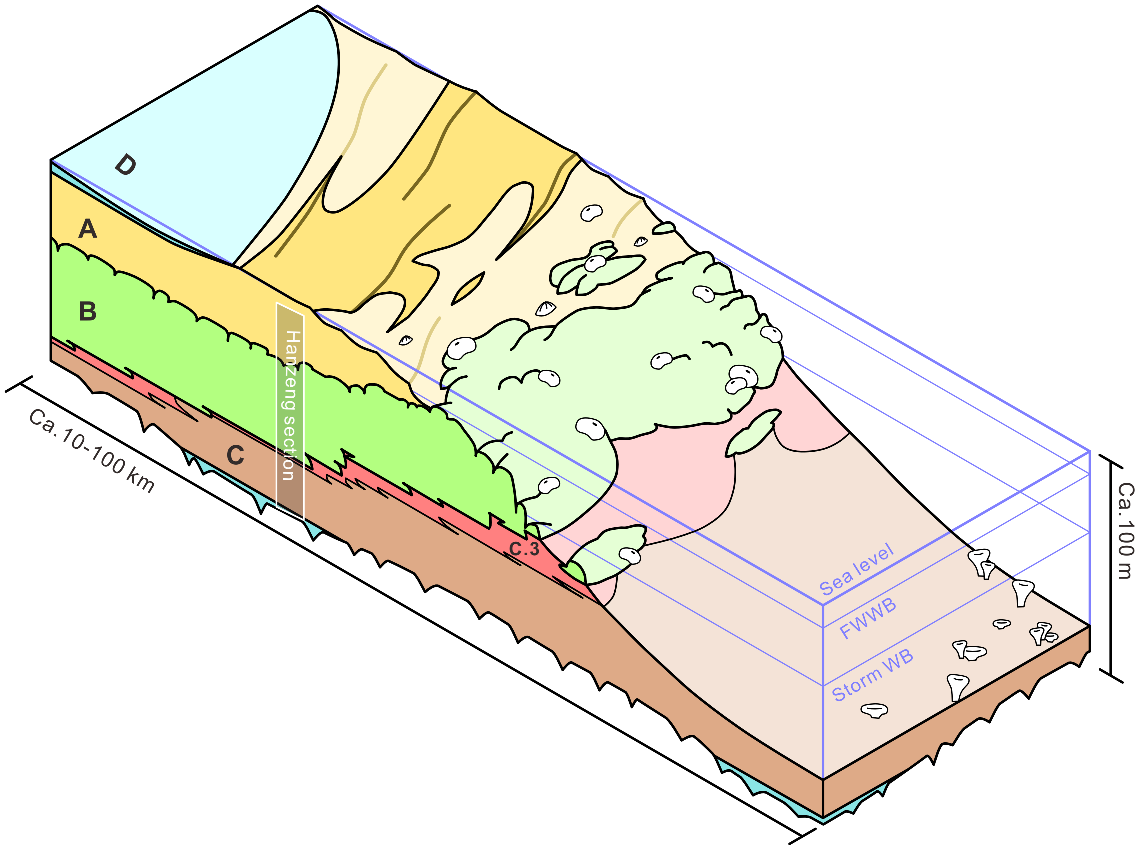

D
A
B
C
C.3
Hanzeng section
Ca.10-100 km
Ca.100 m
Sea level
FWWB
Storm WB


1a
1b
2
3a
3b
4a
4b
5a
5b
5c

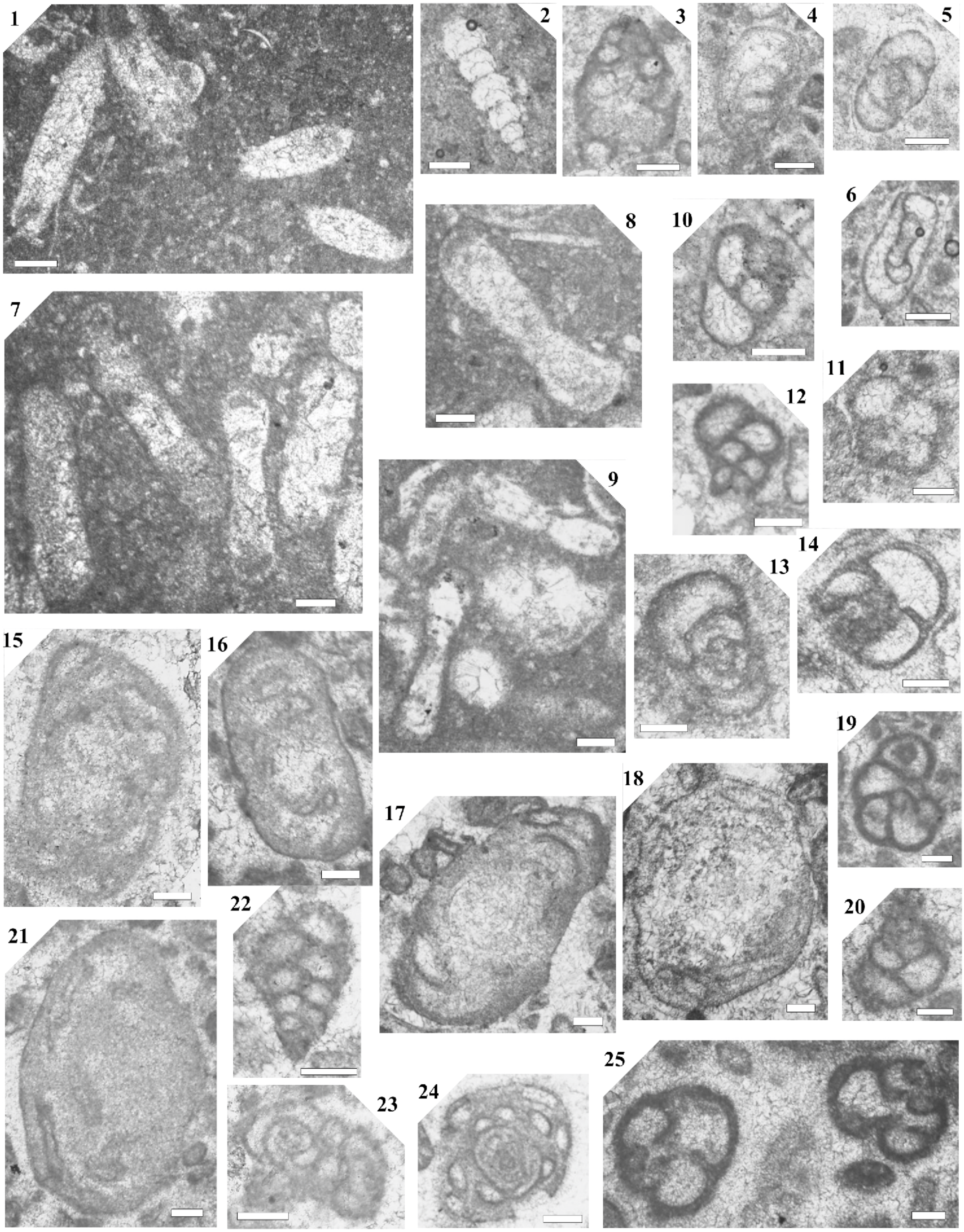
1
2
3
4
5
6
7
8
9
10
11
12
13
14
15
16
17
18
19
20
21
22
23
24
25

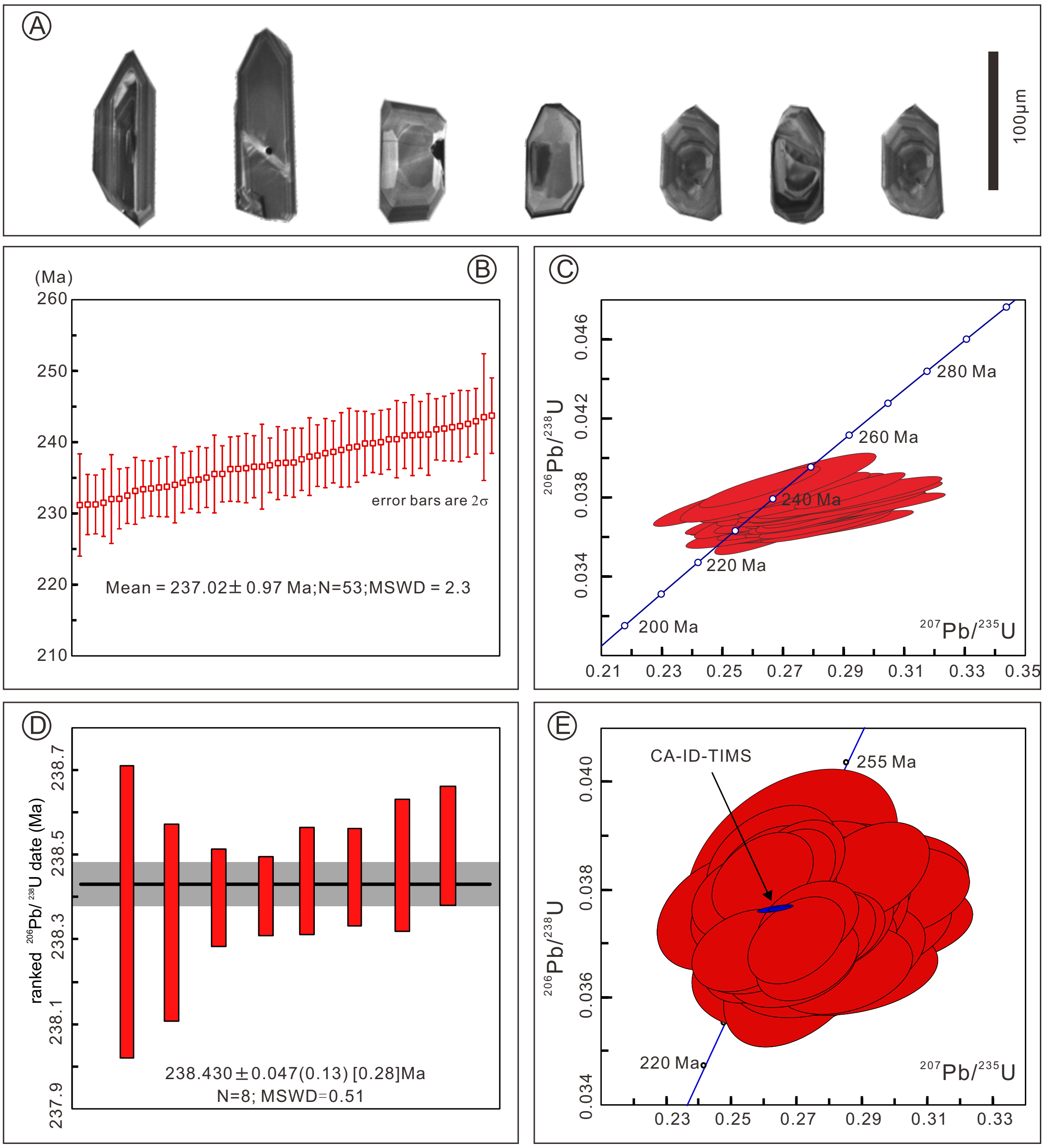

A
100μm
B
(Ma)
260
250
240
230
220
210
error bars are 2σ
Mean = 237.02± 0.97 Ma;N=53;MSWD = 2.3
C
206Pb/238U
0.046
0.042
0.038
0.034
280 Ma
260 Ma
240 Ma
220 Ma
200 Ma
207Pb/235U
0.21
0.23
0.25
0.27
0.29
0.31
0.33
0.35
D
ranked 206Pb/238U date (Ma)
238.7
238.5
238.3
238.1
237.9
238.430±0.047(0.13) [0.28]Ma
N=8; MSWD=0.51
E
CA-ID-TIMS
255 Ma
220 Ma
206Pb/238U
0.040
0.038
0.036
0.034
207Pb/235U
0.23
0.25
0.27
0.29
0.31
0.33

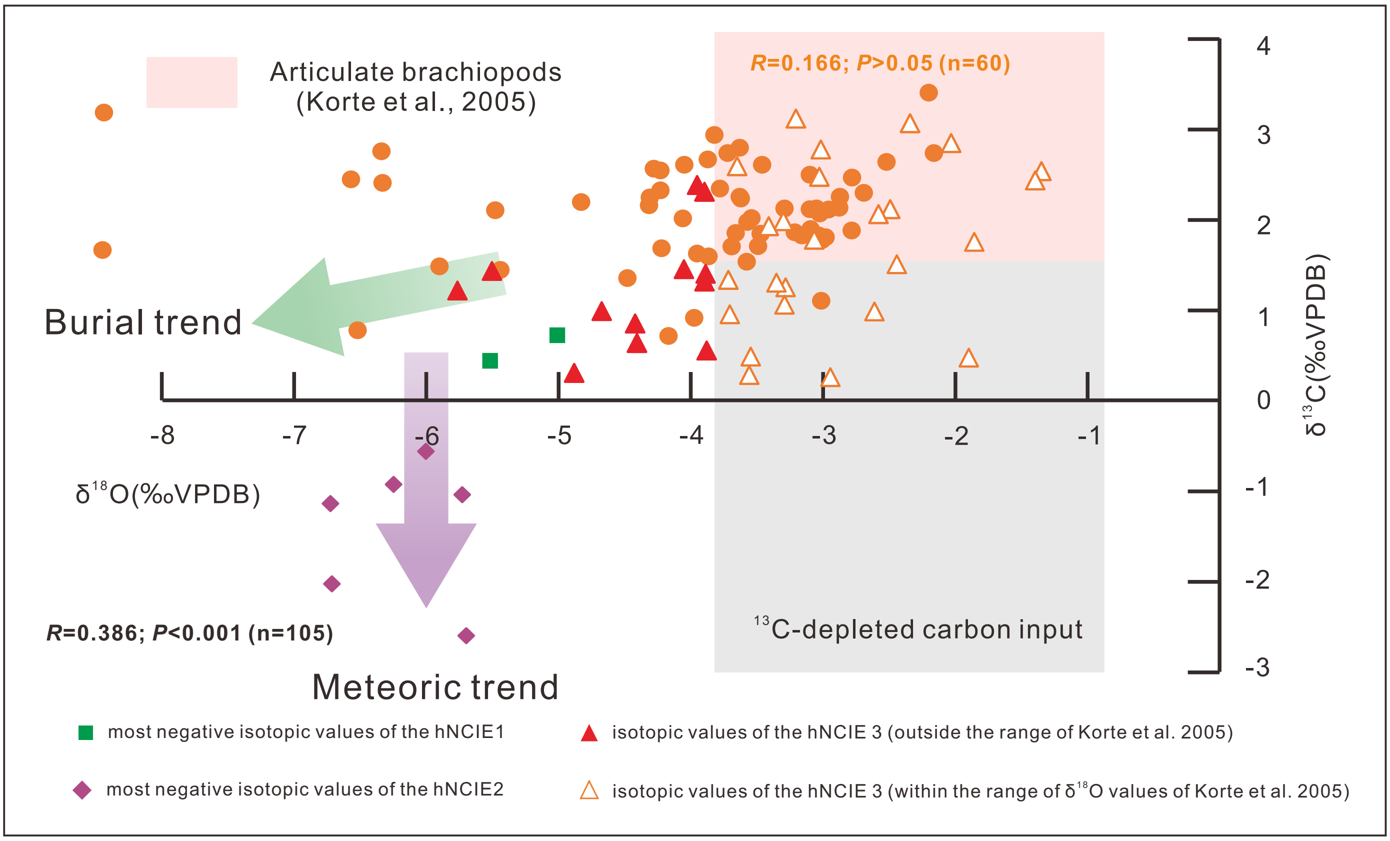

Articulate brachiopods
(Korte et al., 2005)
R=0.166; P>0.05 (n=60)
Burial trend
Meteoric trend
R=0.386; P<0.001 (n=105)
13C-depleted carbon input
δ18O(‰VPDB)
δ13C(‰VPDB)
-8
-7
-6
-5
-4
-3
-2
-1
4
3
2
1
0
-1
-2
-3
most negative isotopic values of the hNCIE1
most negative isotopic values of the hNCIE2
isotopic values of the hNCIE 3 (outside the range of Korte et al. 2005)
isotopic values of the hNCIE 3 (within the range of δ18O values of Korte et al. 2005)

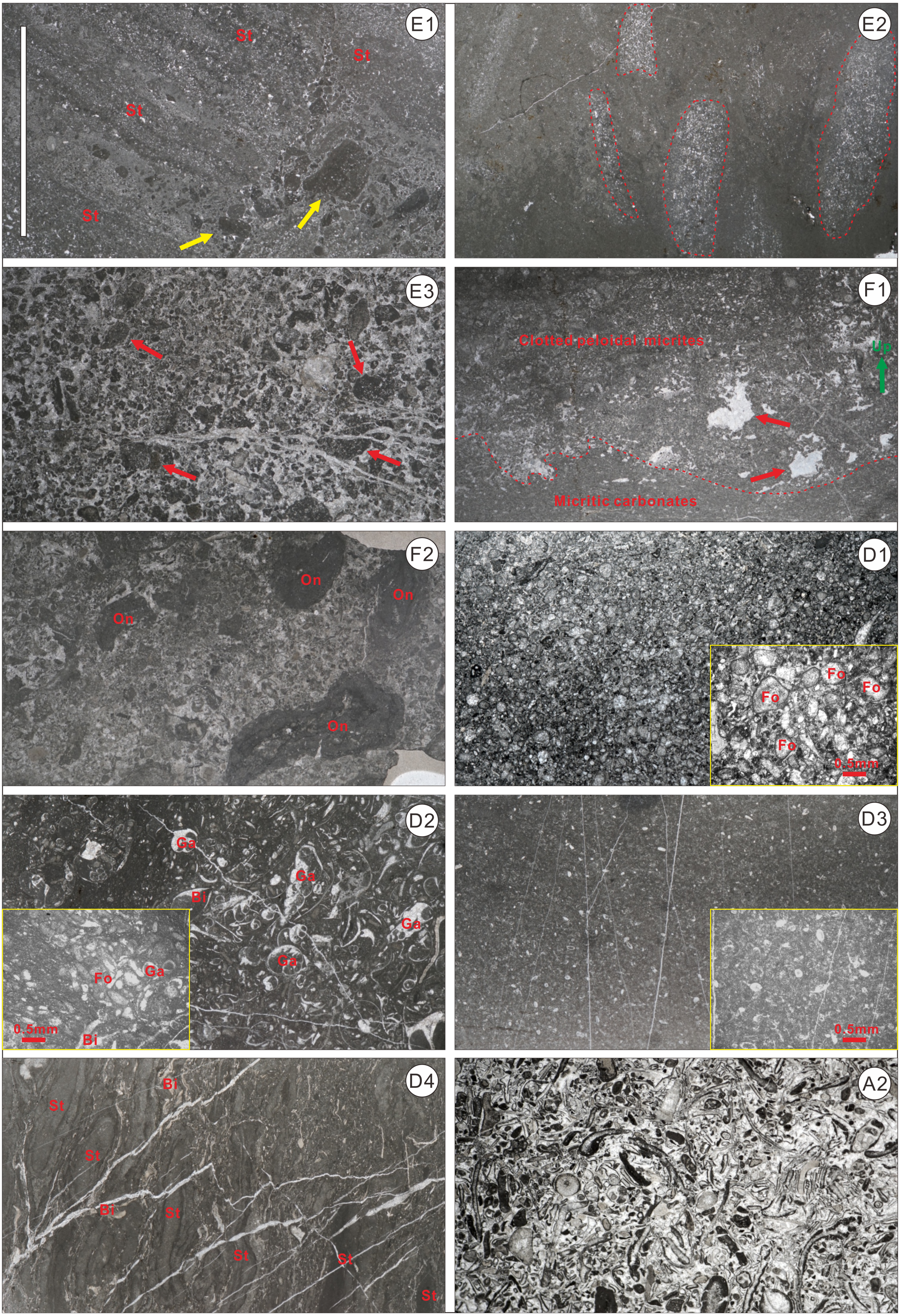

E1
St
St
St
St
E2
E3
F1
Clotted peloidal micrites
Up
Micritic carbonates
F2
On
On
On
On
D1
Fo
Fo
Fo
Fo
0.5mm
D2
Ga
Ga
Bi
Ga
Ga
Fo
Ga
0.5mm
Bi
D3
0.5mm
D4
Bi
St
St
Bi
St
St
St
St
A2

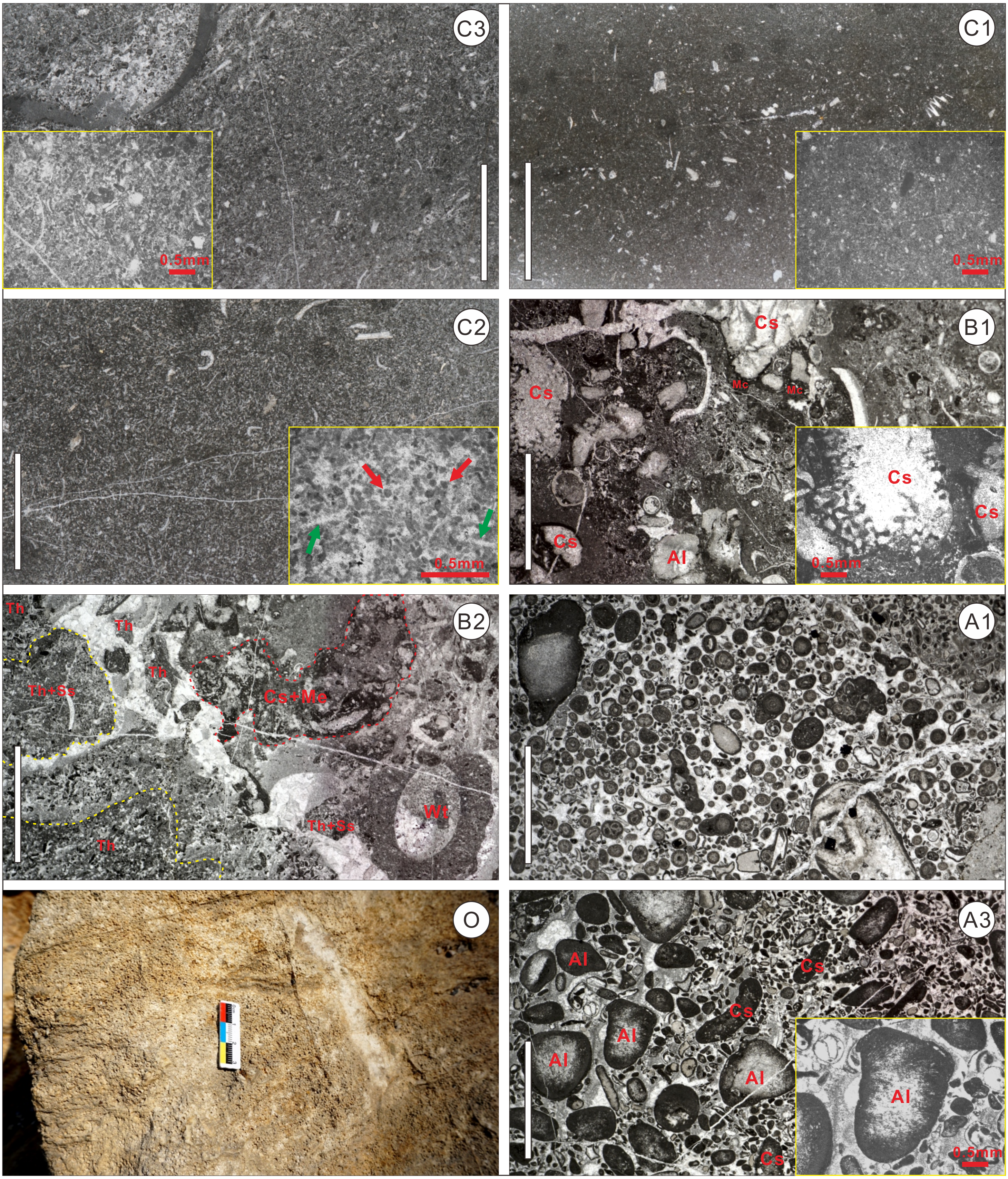
C3
0.5mm
C1
0.5mm
C2
0.5mm
B1
Cs
Mc
Mc
Cs
Cs
Al
Cs
Cs
0.5mm
B2
Th
Th
Th+Ss
Th
Cs+Me
Th+Ss
Wt
Th
A1
O
A3
Al
Cs
Cs
Al
Al
Al
Cs
Al
0.5mm